Materials Science and Engineering A 551 (2012) 40–49

Contents lists available at SciVerse ScienceDirect

Materials Science and Engineering A

journal homepage: www.elsevier.com/locate/msea

Effect of manganese content and microstructure on the susceptibility of X70 pipeline steel to hydrogen cracking

D. Hejazi [a,*], A.J. Haq [a], N. Yazdipour [a], D.P. Dunne [a], A. Calka [a], F. Barbaro [b], E.V. Pereloma [a]

[a] School of Mechanical, Materials & Mechatronic Engineering, University of Wollongong, Wollongong, NSW 2522, Australia
[b] BlueScope Steel Limited, Five Islands Rd, Port Kembla, NSW 2505, Australia

ARTICLE INFO

Article history:
Received 5 January 2012
Received in revised form 26 March 2012
Accepted 11 April 2012
Available online 1 May 2012

Keywords:
Pipeline steel
Microstructure
Hydrogen charging
Fracture toughness
Fractography
Inclusions

ABSTRACT

The influence of composition and microstructure on susceptibility to hydrogen induced cracking (HIC) was investigated in high strength pipeline steels, with Mn contents of 1.2% (standard, X70), and 0.5% (medium, MX70). The HIC resistance of the simulated coarse grained heat affected zone microstructures and normalized X70 transfer bar was also investigated. Notched and fatigue pre-cracked samples were charged with hydrogen prior to three point bend tests.

The conditional fracture toughness J_Q was determined. The results are discussed in relation to grain size, microstructure, composition and the type and distribution of non-metallic inclusions and precipitates.

1. Introduction

Over the last 20 years in Australia the standard gas pipeline grade has moved from X52 through to the present X70, with the maximum operating pressure rising from 6.8 MPa to 15.3 MPa. Higher strength steels allow economic benefits through the use of thinner walled pipe, with lower costs for transport-to-site and field welding; and/or higher operating pressures with lower gas transportation costs [1].

Pipeline steels can contain small concentrations of hydrogen because of absorption during pipe welding or as a result of environmental exposure. The presence of hydrogen raises the possibility of hydrogen induced cold cracking (HICC or HIC) [2]. When a steel pipeline is exposed to an acidic environment, its surface corrodes and produces hydrogen. In the case of sour gas, the presence of H_2S can retard the recombination of hydrogen atoms to form hydrogen molecules, allowing hydrogen atoms to enter the steel. The adsorbed hydrogen atoms diffuse to tri-axial stress zones and become trapped at sensitive microstructural features such as hard phases and interfaces between non-metallic inclusions and the steel matrix [3,4]. If the trapped hydrogen reaches the critical concentration necessary for crack initiation, HIC can take place. The absorbed hydrogen atoms can also recombine to form molecules at defect sites such as voids, inclusions, grain boundaries and dislocations, resulting in pressure build up that can lead to blisters and/or cracking [5].

Understanding of the mechanisms of HIC of steels has been enhanced by the development of models for hydrogen-trapping by microstructural features, with local accumulation of hydrogen [6]. A variety of structural features can act as traps: e.g., grain boundaries, microvoids, dislocations, non-metallic inclusions and precipitate particles [7]. These traps can be reversible or irreversible depending on their binding energy for hydrogen atoms. Grain boundaries and dislocations are weak traps with low binding energies. On the other hand, the interfaces of non-metallic inclusions such as MnS, oxides and oxysulphides of Al and Ca, and precipitates like TiC are considered to be strong irreversible traps for hydrogen at normal service temperatures [2,8–10]. Inclusions and precipitates that have been reported in pipeline steels include Al_2O_3, complex Al–Ca–Si-oxides, oxides and oxysulphides of Ca and Al, oxides of Mg and Mn, the spinel-type double oxide $FeO{\cdot}Al_2O_3$, titanium oxide, ferric carbide, MnS, complex (Fe, Mn)S and nitrides and carbonitrides of Ti and Nb [2–4,6,11–16]. Large inclusions such as elongated MnS and clusters or stringers of oxides have been reported to increase the susceptibility of steels to HIC [17] and hydrogen-induced blister cracking has been observed in pipeline steels for Mn > 0.3% on exposure to a sour gas environment [18]. However, a quench-tempering treatment has been reported to remove the detrimental effect of Mn [19]. Elongated MnS inclusions can degrade the fracture toughness of both the pipe body and

* Corresponding author. Tel.: +61 2 42215718; fax: +61 42215474.
E-mail address: dh712@uowmail.edu.au (D. Hejazi).

0921-5093/$ – see front matter © 2012 Elsevier B.V. All rights reserved.
http://dx.doi.org/10.1016/j.msea.2012.04.076

Table 1
Chemical composition of the steels (wt.%).

	C	P	Mn	Si	Ni	Cr	Mo	Cu	Al	Nb	Ti	V	Ca	N	$C_{E(IIW)}$
X70	0.074	0.012	1.14	0.22	0.024	0.029	0.1	0.023	0.019	0.06	0.02	0.002	0.0002	0.0041	0.293
MX70	0.085	0.01	0.5	0.19	0.018	0.26	0.11	0.011	0.04	0.059	0.035	0.003	0.001	0.0054	0.245

the weld line; and they can seriously reduce the cracking resistance in the presence of hydrogen [20]. However, elongated MnS inclusions can be eliminated in conventional high Mn steels by use of low S levels and sulphide shape controlling additions of Ca [21].

In recent years, there have been attempts to shift to lower Mn levels, in the range of 0.2–0.5% to reduce susceptibility to HIC, as well as decreasing centerline microstructural banding. At these lower levels of Mn and at a given S level, formation of MnS from the liquid will take place closer to the solidification temperature and thus the particles are smaller in size [22]. Since the plasticity of MnS inclusions in the hot rolling process increases directly with increasing Mn level [21], lowering the Mn level should reduce the deformability of the inclusions, thereby reducing the final aspect ratio.

The steel microstructure also plays an important role in HIC. In the thermo-mechanically controlled processing (TMCP) of pipeline steels, a range of microstructures can be obtained, which are based on polygonal, quasi-polygonal or bainitic ferrite, together with one or more of the minor constituents: pearlite, bainite, martensite and austenite [23–25]. It has been reported that the efficiency of trapping tends to increase in the following order: small second phase particles, coarse pearlite, fine pearlite, bainite, and martensite [15,26]. Huang [3] reported that microstructures containing granular bainite with martensite/austenite (M/A) micro-constituent increase the susceptibility to HIC. Granular bainite forms at relatively high transformation temperatures and, as the cooling rate increases, transformation occurs at lower temperatures, producing finer bainitic ferrite laths with finer MA islands aligned along lath boundaries [23]. This ferritic product also has a higher dislocation density and higher strength than ferrite formed at higher temperatures [23,27–31].

This study was conducted with the aim of investigating the effect of microstructure and composition on HIC of X70 pipeline steels with standard (1.2 wt.%) and medium (0.5 wt.%) Mn contents. The program involved cathodic hydrogen charging (2 and 4 ppm), three-point bend tests and microstructural characterization. The coarse grained heat affected zone (CGHAZ) was also simulated and tested for HIC resistance compared with the hot rolled (parent) samples.

2. Experimental

Standard and medium Mn X70 grade pipeline steels (X70 and MX70, respectively) were provided by BlueScope Steel Ltd. for use in this investigation. Samples were taken from the X70 transfer bar (TB) and from the finish rolled X70 and MX70 steels. The chemical compositions of the steels are listed in Table 1. The carbon equivalents were calculated using the IIW formula [32]. The transfer bar samples were normalized in an argon atmosphere at 950 °C for 20 min to homogenize the structure before testing.

The CGHAZ structure typical of pipeline welding conditions was simulated using a Gleeble 3500 thermomechanical simulator. Samples were subjected to a cooling time of 3 s between 800 °C and 500 °C ($\Delta t_{8\to5}$), consistent with that obtained for a heat input of 0.77 kJ/mm on 10 mm thick linepipe, see Fig. 1. High-pressure Ar gas was used for cooling. The hardness of the steels was characterized by Vickers hardness testing using an INDENTEC instrument at a load of 20 kg.

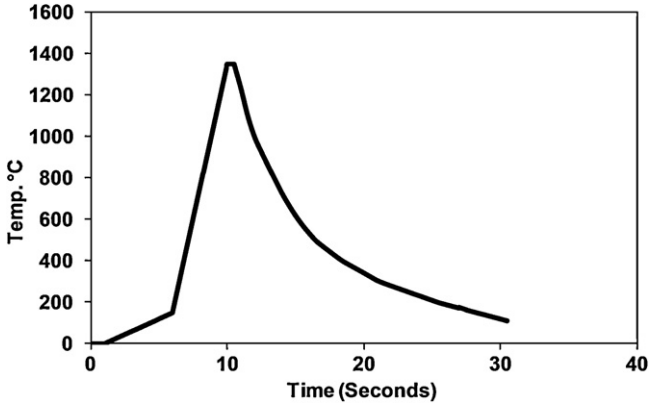

Fig. 1. Thermal cycle used for simulation of the coarse grained HAZ structure produced during in-service pipeline welding.

Samples of dimensions 5 mm × 5 mm × 25 mm were cut with the long direction (L) in the rolling direction of the bar or strip. A 1 mm deep, 0.3 mm wide notch was wire cut so that the notch plane included the short transverse direction (S), and the notched test piece had an L–S configuration [33]. The notched samples were then subjected to fatigue pre-cracking on an Instron 1341 machine. The Syncrack software (Syncrack Version 1, developed by Arthur Carlton Synapse Technology Pty Ltd.) was employed to carry out cyclic loading. The load used for pre-cracking, P_L, is a function of yield strength and is given by Eq. (1) [34]

$$P_L = \left[\left(\frac{4}{3}\right)\left(\frac{Bb_0^2\sigma_Y}{S}\right)\right] \quad (1)$$

where B, b_0, S and σ_Y are effective thickness, original uncracked ligament, span and effective yield strength, respectively. To obtain a fatigue crack of 1.5 mm depth, maximum loads of 850 N and 1350 N were applied for the as-received and HAZ samples respectively. The stress ratio and cycling frequency were 0.4 and 50 Hz respectively. A range of 50,000–100,000 cycles was used for each specimen [35]. The machine cross-head speed during the three point bend test was 0.0083 mm/s.

Electrochemical charging was performed immediately after fatigue pre-cracking to ensure that the charging was carried out on fresh surfaces. Cathodic hydrogen charging of the samples at a current density of 50 mA/cm^2 was performed in 0.5 N H_2SO_4 with 250 mg/L of $NaAsO_2$ as a recombination poison. Calibration curves were obtained by charging the samples for different times. To prevent the loss of hydrogen, the samples were stored in liquid nitrogen immediately after cathodic charging. The amount of hydrogen charged was measured by hot extraction, using an Eltra ONH-2000 [36]. The distribution of hydrogen may be inhomogeneous because it diffuses from the surface into the material during charging and effuses from the surface after charging. Therefore, hydrogen measurement was performed on samples taken out from a small localized region (~2 mm × 2 mm × 5 mm) of the charged samples around the crack tip. This is the region where the crack grows during three point bend testing and hence is most relevant to the fracture toughness results presented. The calibration curve showed that 20 and 90 min of charging were required to introduce 2 and 4 ppm of hydrogen, respectively.

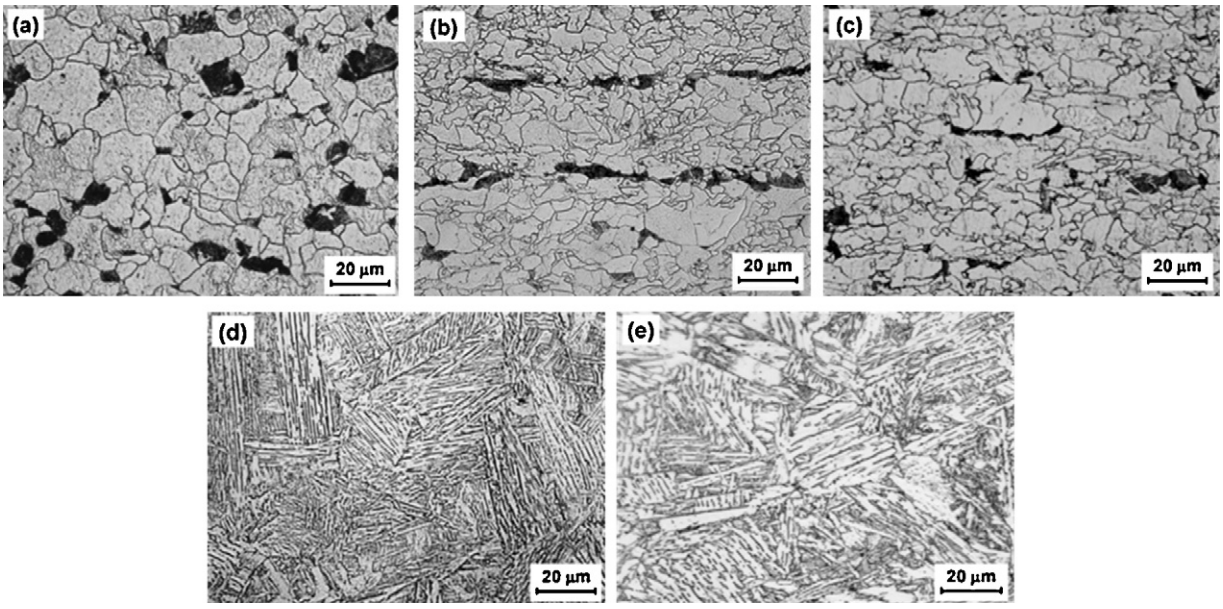

Fig. 2. Optical micrographs of samples. (a) Normalized standard Mn transfer bar, (b) X70 strip, (c) MX70 strip, (d) X70 HAZ and (e) MX70 HAZ.

In order to minimize hydrogen loss three point bend tests were conducted using a Instron 5566 machine within 10 min of charging. The samples were subjected to a series of loading–unloading cycles and load vs. load line displacement curves were obtained. Crack extension was calculated from the load line displacement as follows (Eq. (2)):

$$a = W \times (0.997 - 3.58U - 1.51U^2 - 110U^3 + 1232U^4 - 4400U^5) \quad (2)$$

where a is the crack length, W is the sample width and U is given by Eq. (3).

$$U = \frac{1}{1 + \sqrt{EB\delta/F}} \quad (3)$$

where δ, E, B and F are crack opening displacement, the elastic modulus, sample thickness and the applied load respectively. The data collected by a digital camera during the three point bend tests were used to measure δ. The J integral vs. crack extension curves were obtained in accordance with the method specified in ASTM E813-89 [34] and the conditional value of fracture toughness, J_Q, was calculated.

The microstructures of all samples were characterized using standard optical metallographic techniques. The polished samples were etched using 2% nital solution and examined by optical microscopy. Energy dispersive X-ray spectroscopy (EDS) analysis of the samples was carried out using a JEOL JSM-7001F field emission gun scanning electron microscope (FEGSEM). To analyze the type and distribution of inclusions and precipitates, automated electron beam particle analyser software, Esprit Steel (Bruker, Germany), was employed. An area of 5 mm × 2 mm of each sample was scanned. After the three point bend test, the fracture surfaces of the samples were examined using a JEOL JSM 6490LV SEM in a region within 1 mm of the root of the fatigue crack in order to achieve the best correlation.

3. Results

3.1. As received material characterization

3.1.1. Optical metallography and precipitate characterization

Fig. 2 shows optical micrographs of the samples investigated. The normalized TB sample (Fig. 2a) exhibited a ferrite–pearlite microstructure with an average ferrite grain size of 14 ± 0.5 μm. Although the X70 and MX70 strips also showed ferrite–pearlite microstructures, the grains were slightly elongated along the rolling direction (Fig. 2b and c). The average sizes of the ferrite grains were 10 ± 0.8 and 11 ± 0.6 for the X70 and MX70 strip steels. The area fraction of pearlite was determined to be 12 ± 1, 9 ± 0.8 and 11 ± 1% in the normalized transfer bar, X70 and MX70 samples, respectively. Although there was little difference in the amount of pearlite for the X70 and MX70 steels, pearlite banding was more evident in the hot rolled X70 strip, consistent with its higher Mn level and more pronounced compositional segregation. The simulated CGHAZ of the X70 and MX70 (Fig. 2d and e) consisted mainly of a bainitic ferrite microstructure that formed from coarse-grained austenite.

The number of precipitate particles per square mm was determined using SEM with particles ≥0.25 μm being counted. Since the number of particles per mm^2 was found to be significantly higher in the MX70 sample (77 mm^{-2}) than in X70 (38 mm^{-2}), the standard X70 steel is much "cleaner" than the medium Mn version, in terms of density of inclusions/precipitates. The results of EDS microanalysis of the precipitates are shown in Fig. 3, which is a plot of the numbers of the different types of precipitates detected in the test area for the two steels. A major difference, evident in this plot, is that the areal density of nitrides in MX70 was more than an order of magnitude higher than for X70. Most of these nitrides were complex (Ti,Nb)(C,N) precipitates. This striking difference between the standard and medium Mn steels is likely to be due to the higher Ti, C and N contents of the MX70 steel (Table 1), which resulted in a significantly larger fraction of carbonitride precipitates. The numbers of sulphide inclusions per unit area, particularly MnS and complex MnS, were almost the same for both steels. Since the S contents of the two steels were the same (0.002%) and both Mn contents are well in excess of that required for the stoichiometric ratio (Mn:S = 1.71:1), the volume fractions of sulphides in the

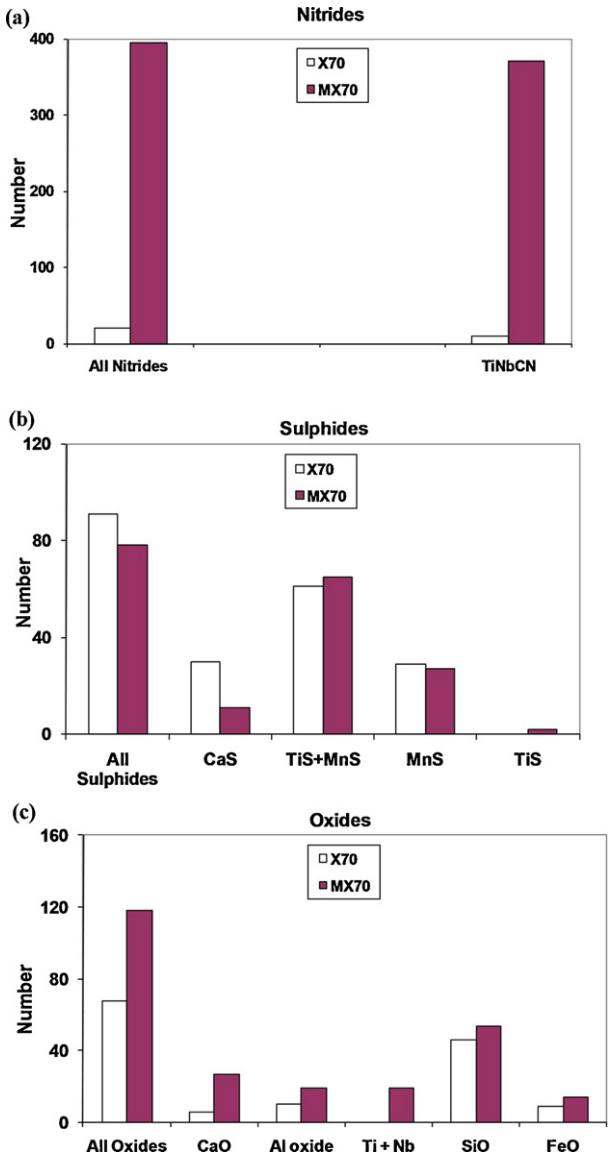

Fig. 3. Plots showing the number per unit area and types of (a) nitrides, (b) sulphides and (c) oxides present in the two steels.

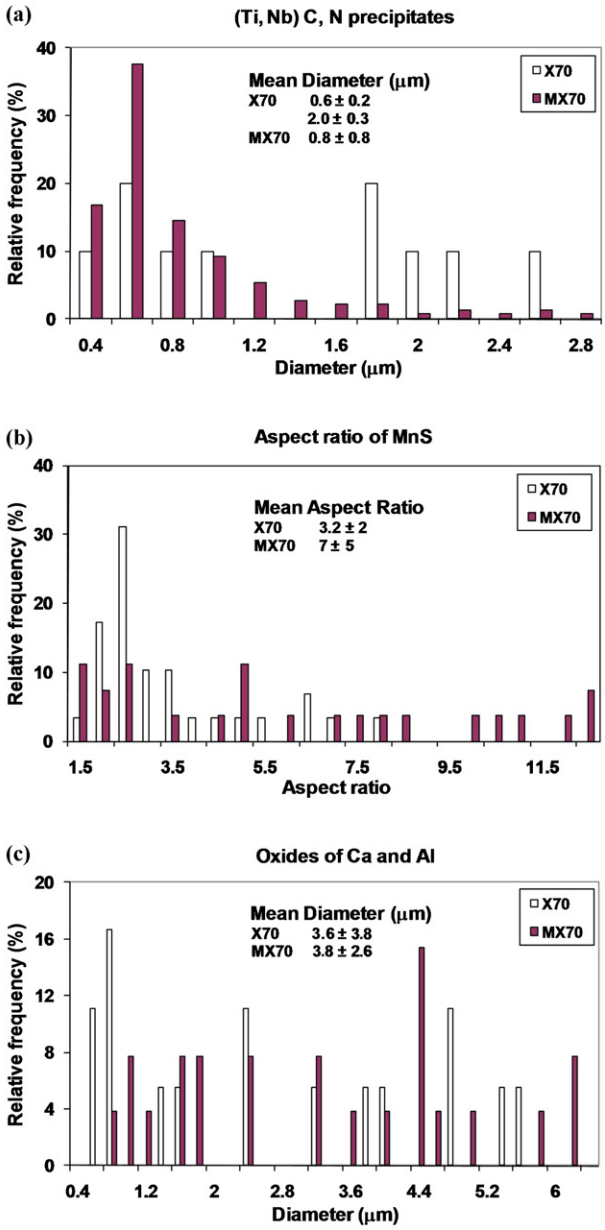

Fig. 4. Plots showing the mean values and distribution of (a) size of (Ti,Nb)(C,N) precipitates, (b) aspect ratio of MnS and (c) size of oxides of Ca and Al.

two steels would be expected to be approximately the same. The volume fractions were not determined, but the total numbers of S-containing precipitates per unit area were similar for the two steels (Fig. 3b). In contrast, the number of oxides in the MX70 strip was almost double that observed for the X70 strip. These oxide inclusions usually contained Fe, Ca, Al, Mg and Mn, and a small amount of Ti was present in about 50% of these precipitates.

The mean sizes and the size distributions of the (Ti,Nb)(C,N), Ca–Al oxides, and the aspect ratio of MnS precipitates in the two steels are shown in Fig. 4. The (Ti,Nb)(C,N) precipitates in MX70 strip exhibited a unimodal distribution with an average diameter of $0.8 \pm 0.8\ \mu m$. The size distribution of the precipitates was very broad with a long tail (not shown in Fig. 4a), with some precipitates having diameters in the range 3–5 μm. On the other hand, the X70 strip showed a bimodal distribution with mean sizes of 0.6 ± 0.2 and $2 \pm 0.3\ \mu m$. However, it should be noted that the number of the nitrides per unit area for the MX70 sample was significantly higher than that for the X70 strip.

The mean aspect ratio of MnS particles in the MX70 strip was larger than that of the X70 strip. The distribution of aspect ratios of MnS particles in the MX70 strip was also wider and had a long tail (Fig. 4b). Although the aspect ratio for MnS particles in MX70 extended up to about 20:1, the mean ratio was 7 ± 5. For X70, the mean aspect ratio was 3.2 ± 2. The present results are not consistent with the reported trend of reduced plasticity and lower aspect ratio of MnS particles with decreasing Mn content [21].

The average sizes of the Ca–Al oxide precipitates in the X70 and MX70 strips were similar: $3.6 \pm 3.8\ \mu m$ and $3.8 \pm 2.6\ \mu m$, respectively. Compared to the carbonitrides, the standard deviations of the average values of the diameters of the oxide inclusions and the aspect ratios of MnS precipitates were relatively high, because these particles were less abundant and showed a considerable spread in particle size/aspect ratio.

3.1.2. Hardness profile

Fig. 5 shows the hardness profiles of the two steels after HAZ simulation. The gradients indicate that the simulated CGHAZ extended over a distance of about ±10 mm from the sample center. The approximately constant hardness of this central zone was

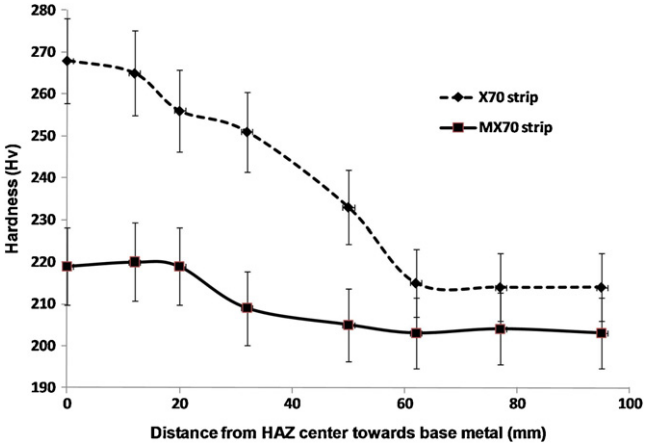

Fig. 5. Hardness profiles of X70 and MX70 samples subjected to weld thermal cycle simulation.

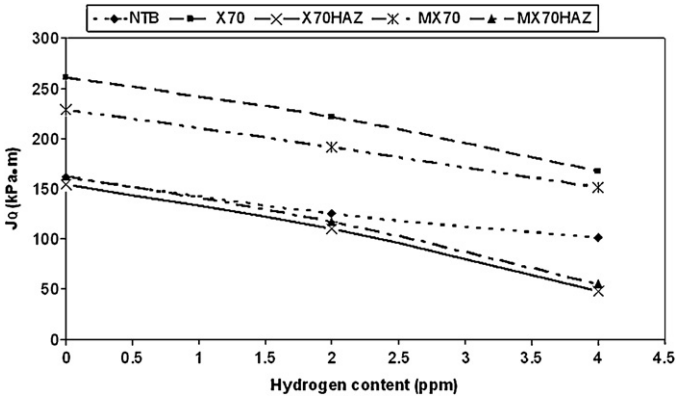

Fig. 8. Variation of J_Q values with hydrogen content for the tested samples.

about 265 HV for X70 and 222 HV for MX70, indicating that, for the same cooling rate, the X70 transformed to a structure with a higher strength than the MX70 steel. The X70 CGHAZ region exhibited a hardness about 50 HV points higher than the base metal, whereas the difference was ~20 HV points for MX70. The higher hardness increment for the X70 HAZ sample indicates transformation at a lower temperature to finer and more dislocated bainitic ferrite. The finer lath structure for the X70 HAZ sample is evident in Fig. 2 (compare Fig. 2d and e). In the hot rolled condition, the X70 was about 10 HV points higher than MX70, but the difference was amplified to 43 HV points for the simulated CGHAZ samples. Li et al. [8] reported a similar simulated CGHAZ hardness for X70 grade steel (238 HV), for the same peak temperature (1350 °C) and $\Delta t_{8\rightarrow5}$ = 4 s (c.f. 3 s in the current work). The alloy composition was: 0.05 C, 0.26 Si, 1.48 Mn, 0.17 Mo, 0.05 Nb ($C_{E(IIW)}$ = 0.3).

3.2. Three point bend test

Figs. 6 and 7 show the *J*–resistance (*J*–R) curves (*J*-based fracture resistance curves) for all samples, before and after hydrogen charging. The calculated J_Q values are given in Table 2 and are plotted in Fig. 8. The values of J_Q decreased with increasing hydrogen content in all cases with the decrease being approximately linear, Fig. 8. Assuming a linear relationship between *J* and [*H*], the gradients (in MPa m/ppm H) for X70 and MX70 are approximately −23 and −19,

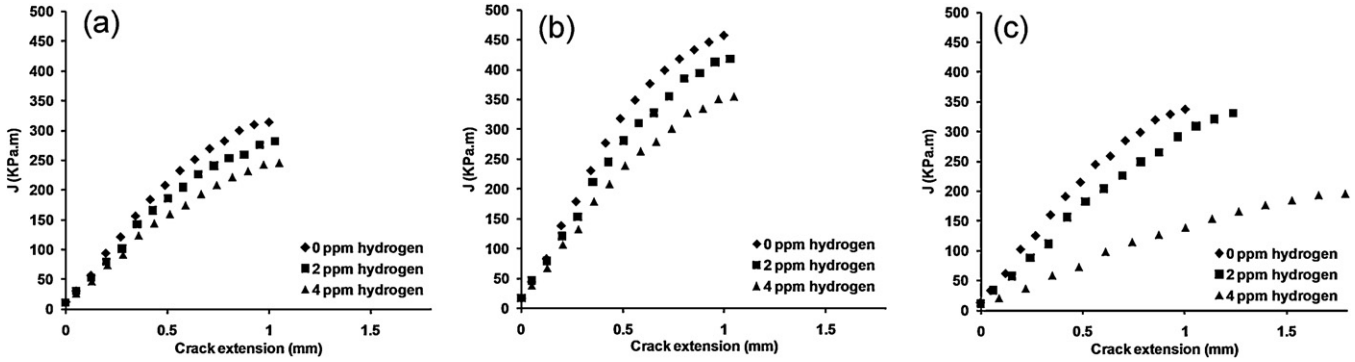

Fig. 6. *J*–*R* curves for X70 samples, before and after charging to 2 and 4 ppm hydrogen: (a) normalized standard Mn transfer bar; (b) hot rolled strip; and (c) simulated CGHAZ.

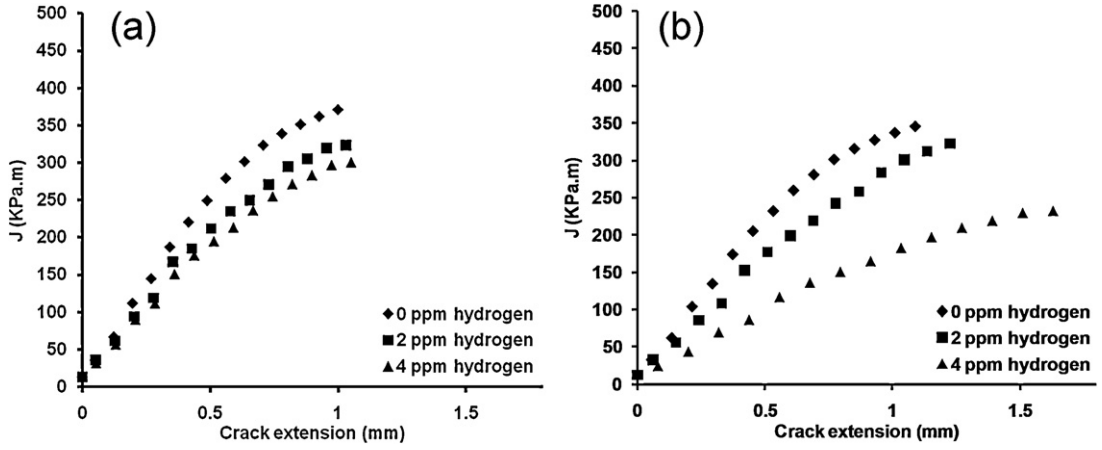

Fig. 7. *J*–*R* curves for MX70 samples, before and after charging to 2 and 4 ppm hydrogen: (a) hot rolled strip; and (b) simulated CGHAZ.

Table 2
Experimental values of fracture toughness, J_Q before and after charging to 2 and 4 ppm hydrogen.

Hydrogen content (ppm)	X70 transfer bar	X70 strip	MX70 strip	X70 strip HAZ	MX70 strip HAZ
0	162	261	229	155	163
2	125	222	192	110	117
4	101	168	152	48	55

respectively; and −15 for the normalized transfer bar sample and −27 for both of the simulated HAZ samples.

The hot rolled X70 samples clearly exhibited the highest fracture toughness, Figs. 6 and 8. The J_Q values for the normalized transfer bar showed a similar dependence on hydrogen content, but the magnitudes of the J_Q values were considerably lower than for the hot rolled strip, Fig. 8. Comparison of the J_Q values for the standard and medium Mn strips (Figs. 6b, 7a and 8) indicates that the uncharged and charged MX70 samples were slightly, but consistently lower than those for the X70 strip.

The simulated CGHAZ structures of the X70 and MX70 steels showed significantly lower J_Q values than those of the hot rolled strip steels. These results demonstrate that there was a significant reduction in the toughness of both steels when the fine grained ferrite–pearlite structure of the hot rolled steels was replaced by a coarse bainitic ferrite structure with martensite–austenite islands, that was produced by transformation of coarse austenite grains.

3.3. Fractography

Typical SEM images of fracture surfaces of the normalized TB and the two hot rolled strip steels, before and after charging, are presented in Fig. 9. The uncharged samples exhibited features characteristic of ductile fracture, such as shear dimples and microvoids, Figs. 9d and g [7,37,38]. However, the hot rolled X70 and MX70 strips exhibited a combination of dimples and microvoids, whereas the normalized transfer bar sample showed only elongated dimples without any microvoids, Fig. 9a. The fracture surface of the MX70 sample presented in Fig. 9g contains a large inclusion within a large shear/tear dimple.

On charging with 2 ppm hydrogen, the normalized transfer bar and X70 strip specimens showed mixed mode or quasi-cleavage fracture, but with cleavage dominating in the case of normalized transfer bar (Fig. 9b) and elongated dimples without microvoids being a significant feature of the X70 strip (Fig. 9e). Furthermore, transverse cracking (cracking perpendicular to the main crack growth direction) was evident in the fracture surface of X70 strip, an effect that was correlated with microstructural banding of pearlite grains parallel to the rolling direction of the strip. With an increase in the hydrogen content to 4 ppm, the fracture appearance of both the normalized transfer bar (Fig. 9c) and X70 strip (Fig. 9f) samples exhibited cleavage fracture with facets containing river markings and shear steps or ridges between facets.

The MX70 strip, on the other hand, showed predominantly elongated shear/tear dimples on charging with 2 ppm H (Fig. 9h); and a fracture surface comprising microvoids and dimples, as well as cleavage facets for 4 ppm hydrogen (Fig. 9i). The charged and uncharged MX70 samples consistently showed inclusions either within dimples or at centers of cleavage fracture regions.

From the fractographs shown in Fig. 9, it is evident that the facets observed in the normalized transfer bar samples are coarser than those in X70 and MX70 strip samples. This difference is likely to arise from the coarser ferrite grain size in the normalized transfer bar samples.

Fig. 10 shows fractographs of simulated CGHAZ samples of X70 and MX70 samples, before and after charging. The uncharged MX70 HAZ sample (Fig. 10d) exhibited a quasi-cleavage morphology with evidence of dimples, microvoids and cleavage facets; whereas only dimples and microvoids were observed for the uncharged X70 HAZ sample (Fig. 10a). Shear dimple regions of the fractured X70 HAZ samples also showed remnants of fine microvoids that had coalesced to produce coarser shear dimples that were 20–50 μm wide. The presence of 2 ppm hydrogen (Fig. 10b and e) resulted in similar quasi-cleavage fracture morphologies in both simulated CGHAZ samples: cleavage facets and regions of microvoids. With 4 ppm hydrogen (Fig. 10c and f), both steels exhibited large cleavage facets separated by shear steps and tear ridges.

4. Discussion

Microstructural features such as reversible and irreversible traps present in the steel reduce the mobility of hydrogen toward regions of stress concentration ahead of the crack tip and thereby influence the susceptibility of the steel to HIC. However, if the hydrogen concentration in the traps increases above the critical value for crack initiation, then traps can act as crack initiation sites. These sites can "trigger" cracking in the stress concentrated zone ahead of the crack front [39]. Micro-fractures around large inclusions were observed in the present work and it is inferred that particle decohesion is induced by trapped hydrogen, producing sharp cracks and a local stress concentration high enough to promote crack extension by cleavage or void growth around the particle. These "pre-cracked" regions become incorporated in the crack surface on propagation of the crack front [39].

The type, amount, size and distribution of traps affect the HIC susceptibility of the steel remarkably [2]. The observed differences in fracture toughness of the different samples studied here are discussed below in terms of the effects of grain size, microstructure and the type and distribution of precipitates.

4.1. Effect of grain size

It is well established that grain refinement of metals and alloys increases the fracture toughness. Consequently, the finer grain size of the X70 strip in the uncharged state results in a higher J_Q value compared with the coarse grained normalized TB. Furthermore, it has also been reported that grain refinement improves the resistance of materials to HIC [40–42]. However, when hydrogen is introduced into the material, grain boundaries can either increase the hydrogen diffusion rate [43–45] or decrease it by acting as reversible hydrogen trapping sites at the nodes [46]. As the grain size decreases, the mobility of hydrogen increases because of a larger grain boundary area per unit volume, but the higher density of nodes or junction points can act as potential traps for hydrogen atoms and lead to a reduction in its overall mobility. As a result of these two opposing effects, the hydrogen diffusion coefficient will be a maximum at an optimum grain size, as pointed out by Ichimura [46]. Since the most significant microstructural difference between the normalized TB sample and the X70 strip was the ferrite grain size, it is likely that in the coarser structure less hydrogen in trapped in nodes and junction points facilitating a higher hydrogen flux to, and build up in, the stress concentrated zone ahead of the crack tip, thus facilitating crack propagation. The fine grained MX70 sample also exhibited higher J_Q values than the TB sample, before and after hydrogen charging.

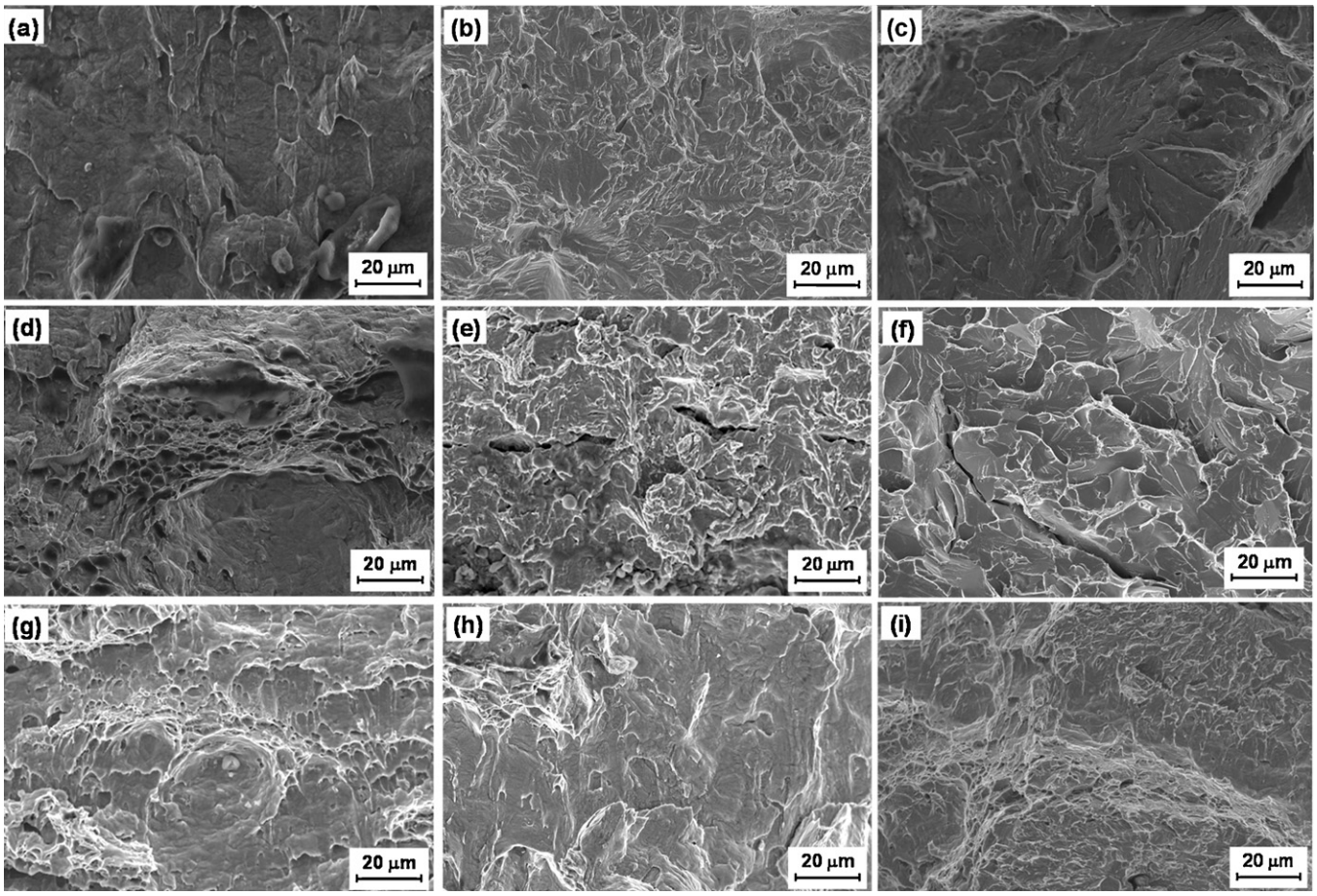

Fig. 9. SEM fractographs of fracture surfaces before and after charging of the samples; left column ((a), (d), (g)) – 0 ppm, middle column ((b), (e), (h)) – 2 ppm, right column ((c), (f), (i)) – 4 ppm: normalized transfer bar – (a)–(c); X70 strip – (d)–(f); and MX70 strip – (g)–(i).

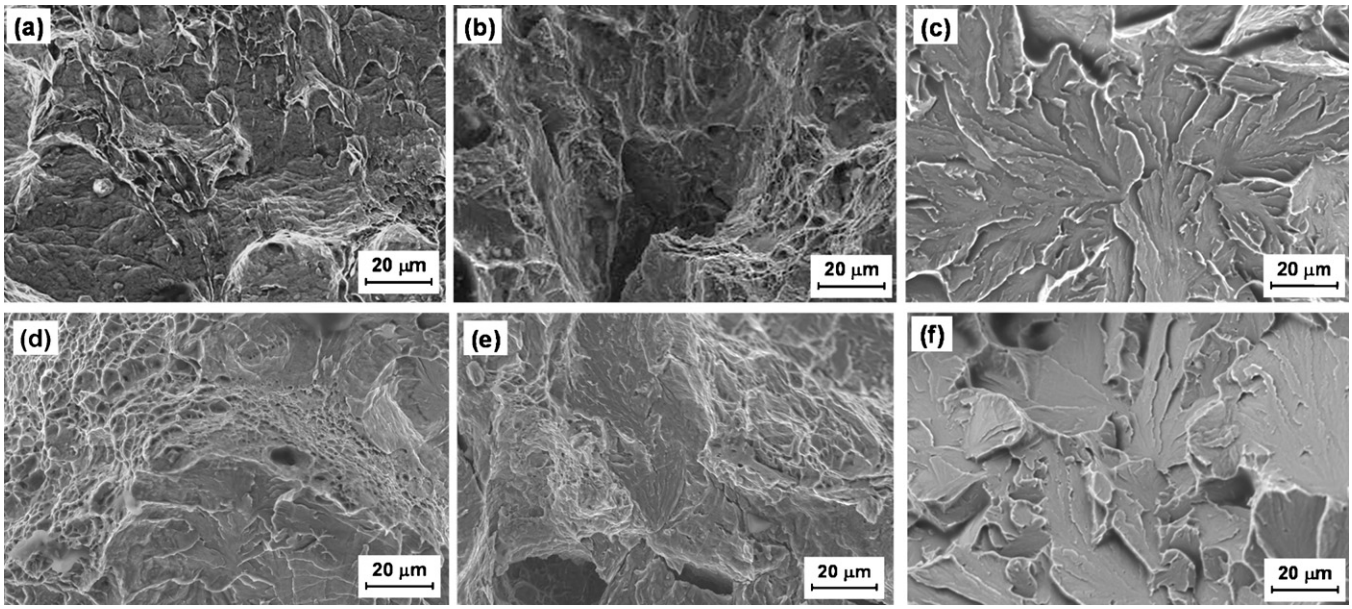

Fig. 10. SEM fractographs of fracture surfaces before and after charging of the simulated CGHAZ samples; left column ((a), (d)) – 0 ppm, middle column ((b), (e)) – 2 ppm, right column ((c), (f)) – 4 ppm: X70 – (a)–(c); and MX70 – (d)–(f).

It is also well known that dislocations can act as effective traps for hydrogen, thereby reducing the mobility of hydrogen atoms. Therefore, the lower dislocation density of the ferrite–pearlite microstructure of the normalized transfer bar sample would also be expected to allow faster diffusion of hydrogen to, and its accumulation in, the stress-concentrated zone ahead of the crack tip. Further, the availability of hydrogen atoms would be likely to facilitate hydrogen build-up in particle/defect traps in close proximity to the crack front. Permeation experiments [47] confirm that the diffusivity of hydrogen is higher in the normalized transfer bar steel compared to the X70 strip. Decohesion or particle cracking would occur when the H concentration and local stress reached critical values. Therefore, in terms of microstructural factors, the lower fracture toughness of the normalized TB sample in the charged state can be attributed to the combined effect of coarser ferrite grains and lower dislocation density. The relatively low fracture toughness in the uncharged condition is considered to be a grain size effect.

4.2. Effect of microstructure

The uncharged and charged X70 strip samples exhibited slightly higher J_Q values than the MX70 samples. A possible contributing factor for this result is that more significant ferrite–pearlite banding was observed for the X70 strip. From electrochemical permeation experiments on ferrite–pearlite banded structures, Chan and co-workers [48,49] have shown that the effective diffusivities of hydrogen in specimens where the banding is perpendicular to the direction of hydrogen entry is an order of magnitude lower than in those specimens where hydrogen entry is along the direction of banding. Since the direction of the loading in the hot rolled X70 strip was perpendicular to the banded structure, reduced mobility of hydrogen toward the crack tip could have contributed to a higher toughness value in charged samples compared with the MX70 strip, which did not show any evidence of banding.

Although the J_Q values in the presence of H were higher for the X70 samples, fracture propagation occurred predominantly by cleavage. Despite this "brittle" mechanism of cracking, more energy was evidently consumed in the crack extension process than for the MX70 samples, which were ostensibly more "ductile", with the dominance of microvoids and shear dimples. Beachem's principle [50], that H induces cracking by facilitating the mechanism to which the microstructure is most susceptible, is relevant to these observations. This principle underpins subsequent development of two general mechanisms for hydrogen embrittlement: hydrogen induced local plasticity (the HELP model [51]); and hydrogen enhanced decohesion (the HEDE model [51]). It is therefore concluded that the lower shear strength of the MX70 and the presence of hydrogen facilitates dislocation motion (local plasticity) that contributes to the formation of microvoids and shear dimples, in association with decohesion/cracking of inclusion and precipitate traps. In comparison with relatively "easy" dislocation movement in MX70, the significantly higher solute Mn content in the X70 could restrict dislocation mobility to the extent that, after fracture initiation by particle decohesion, crack propagation occurs by cleavage, albeit with a higher expenditure of energy. The role of particles is discussed in the following section.

The simulated HAZ microstructures of both samples consisted predominantly of coarse bainitic ferrite laths with aligned interphase martensite–austenite (MA) islands. The boundaries between the bainitic ferrite laths are low angle boundaries that do not impede crack propagation [52]. Fracture of bainitic steels along lath boundaries has been reported [53,54] and the MA constituent is known to provide initiation sites for fracture because of its high hardness and crack susceptibility [55].

When the samples are charged with hydrogen, the bainitic lath boundaries can trap large amounts of hydrogen [15]. Arafin and Szpunar [53] have observed extensive cracking in bainitic microstructures and suggest that the accumulation of a significant amount of hydrogen at the bainitic lath boundaries can eventually lead to the separation of these interfaces and result in cracking when the hydrogen concentration reaches a critical value. Therefore, in the presence of hydrogen, propagation of transgranular cleavage cracks can be facilitated by the presence of bainitic lath interfaces, although the cracks may initiate at local MA regions in the bainitic ferrite structure [53].

The low J_Q values recorded for the simulated CGHAZ samples are a consequence of the coarse prior austenite grain size, the formation of relatively coarse laths of bainitic ferrite, the presence of elongated MA islands, the high hardness of these structures (Fig. 5), and the low resistance to crack propagation along lath boundaries in both the charged and uncharged conditions. The more HIC-resistant structures of the parent X70 or MX70 steels consisted mainly of polygonal or quasi-polygonal ferrite.

The ferrite laths formed in the X70 HAZ sample were finer than those present in MX70 HAZ (Fig. 2d and e), because the higher hardenability of the X70 steel (see $C_{E(IIW)}$ values in Table 1), resulted in transformation on cooling over a lower temperature range. Nevertheless, the J_Q values were only marginally higher for the X70 HAZ (Fig. 8), because lath interfaces and MA islands dominate in the fracture process rather than fracture across the thickness of the laths.

4.3. Effect of precipitates

In hot rolled steels like those used in this study, hydrogen can be trapped at interfaces between the matrix and non-metallic particles or at the surface of voids and cracks, etc. As the trap activation energies of the interfaces of non-metallic inclusions such as MnS and precipitates of TiC are high, they are regarded as strong irreversible traps for hydrogen [9,56,57]. Pressouyre and Bernstein [9] reported that incoherent TiC precipitates are more effective than coherent TiC precipitates, whereas Takahashi et al. [56] and Valentini et al. [58] found fine coherent TiC particles and Ti(C,N) precipitates to be stronger irreversible traps. According to Wei and Tsuzaki [59], NbC precipitates are stronger traps than TiC in tempered martensitic structures and in API X70 steels, subjected to electrochemical charging in H_2SO_4 solutions. Dong et al. [2] have reported that rather than nitrides of Ti and Nb being the main trap sites that cause HIC, coarser inclusions such as oxides play a dominant role. Although Pressouyre and Bernstein [9] considered MnS inclusions to be strong irreversible trapping sites for hydrogen, other researchers have concluded that they have moderate binding energies for hydrogen and can act as reversible trapping sites [60]. The J_Q values for the two strips are discussed below, taking into account relevant reports from the literature and the types and distributions of precipitates observed in this study.

The current study indicated that the MX70 strip had higher number densities of complex (Ti,Nb)(C,N) precipitates and oxides of Ca and Al, compared to the X70 strip (Fig. 3). As mentioned above, several authors reported that fine carbonitrides can act as strong traps for hydrogen and significantly reduce the mobility of hydrogen, thereby increasing its resistance to HIC [61–63]. However, the three point bend tests results showed that the MX70 strip charged to 2 ppm and 4 ppm hydrogen exhibited slightly lower J_Q values than the X70 strip. This result can be rationalized in terms of the size distribution of the different precipitates in these two steels. The carbonitride precipitates in MX70 strip showed a broad distribution of sizes and some very large precipitates were observed (see Fig. 11b). Moreover, the MX70 strip had double the number of oxide inclusions compared to X70 strip with most of the inclusions having diameters greater than 2 μm. Dong et al. [2] observed cracks originating from large inclusions of Ca–Al oxides, rather than

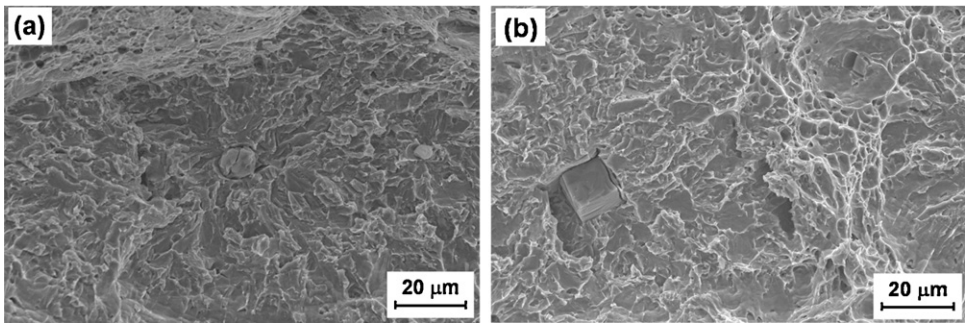

Fig. 11. SEM fractographs of MX70 samples showing large carbonitride particles.

Ti or Nb carbonitrides. They suggested that the larger diameters of the oxides (2–3 μm in diameter) can attract more hydrogen than fine carbonitrides and can therefore play a dominant role in HIC. On this basis, the lower J_Q values observed for the charged MX70 strip may be attributable, at least in part, to the presence of coarse oxide inclusions and/or (Ti,Nb)(C,N) precipitates in these samples. These particles could effectively trap hydrogen to the critical level to induce particle cracking or interfacial decohesion, leading to local void growth and coalescence or to cleavage fracture. This hypothesis is supported by evidence of inclusions/precipitates at the centers of dimples and cleavage fracture sites, see for example, Figs. 9g and 11.

The number densities of MnS precipitates are almost the same in both of these strips. However, it can be seen from Fig. 4b that the distribution of the aspect ratios of MnS precipitates for the MX70 specimen has an extremely long tail with some MnS precipitates exhibiting aspect ratios up to 20:1. Domizzi et al. [11] have reported that the presence of even a small number of very elongated inclusions can result in reduced HIC resistance. So this factor could contribute to the lower HIC resistance of the MX70 steel. However, in this study, the elongated MnS inclusions were aligned perpendicular to the loading direction during the three bend tests and therefore it is suggested that they would not have any significant detrimental effect on fracture toughness of the MX70 strip. Rather, it is considered that the lower J_Q values compared to X70 are due mainly to the presence of a higher total density of precipitates/particles (Fig. 3), particularly oxide inclusions; their susceptibility to H-induced cracking/decohesion; and decreased resistance to shear fracture mechanisms, by dislocation motion, because of the lower concentration of solute Mn.

5. Conclusions

1. Increasing the hydrogen content from 0 to 4 ppm resulted in an approximately linear decrease in fracture toughness (J_Q) for all of the samples tested.
2. The hot rolled X70 steel consistently exhibited higher J_Q values than the MX70 strip before and after hydrogen charging. Therefore, decreasing the Mn content from 1.2% to 0.5% in the steels investigated resulted in a decrease in fracture toughness.
3. In the charged condition, the coarse grained, normalized TB sample showed much lower J_Q values than both hot rolled strip steels. It is concluded that the coarse ferrite grains and the relatively low dislocation density enhanced hydrogen build-up in the stress-concentrated zone ahead of the crack tip, facilitating decohesion and cracking of particles in this zone.
4. The fracture surfaces of X70 and MX70 in the uncharged state were characterized by more ductile modes of cracking: microvoids and shear dimples. In the presence of 2 and 4 ppm hydrogen, more brittle modes: quasi-cleavage and cleavage, were evident.
5. Although the fracture surfaces of hydrogen-charged MX70 showed that shear mechanisms were more significant than for the corresponding X70 samples, MX70 exhibited slightly lower J_Q values than X70. It is concluded that the presence of a higher volume fraction of coarse oxide and carbonitride particles in MX70 promoted H-induced decohesion and the lower yield strength facilitated H-induced local plasticity, with void formation, growth and coalescence.
6. Simulated CGHAZ structures for both the standard and medium Mn steels showed low J_Q values which decreased with increasing hydrogen. There was little effect due to the difference in Mn content. The relatively hard and coarse bainitic-ferrite structure with MA islands resulted in a marked decrease in toughness, both with and without hydrogen.

Acknowledgements

This study was conducted as part of Australian Research Council (ARC) Linkage Grant (LP0883546) with BlueScope Steel Ltd. (BSL) as the industrial partner. The authors would like to thank the ARC and BSL for their financial support. The authors are also grateful to Mr. J. Pelinkas, BSL for hydrogen measurements.

References

[1] P. Venton, Pipeline Construction Costs in Australia, Paper 21, WTIA/APIA Research Panel 7 Seminar, Wollongong, Australia, 1995.
[2] C.F. Dong, X.G. Li, Z.Y. Liu, Y.R. Zhang, J. Alloys Compd. 484 (2009) 966–972.
[3] F. Huang, J. Liu, Z.J. Deng, J.H. Cheng, Z.H. Lu, X.G. Li, Mater. Sci. Eng. A 527 (2010) 6997–7001.
[4] C.F. Dong, Z.Y. Liu, X.G. Li, Y.F. Cheng, Int. J. Hydrogen Energy 34 (2009) 9879–9884.
[5] S.K. Yen, I.B. Huang, Mater. Chem. Phys. 80 (2003) 662–666.
[6] H.B. Xue, Y.F. Cheng, Corros. Sci. 53 (2011) 1201–1208.
[7] E. Villalba, A. Atrens, Eng. Fail. Anal. 16 (2009) 164–175.
[8] S.M. Lee, J.Y. Lee, Acta Metall. 35 (1987) 2695–2700.
[9] Gm. Pressouyre, I. Bernstein, Metall. Trans. A 10 (1978) 1571.
[10] F.G. Wei, K. Tsuzaki, Metall. Trans. A 35A (2004) 3155–3163.
[11] G. Domizzi, G. Anteri, J. Ovejero-García, Corros. Sci. 43 (2001) 325–339.
[12] T.Y. Jin, Z.Y. Liu, Y.F. Cheng, Int. J. Hydrogen Energy 35 (2010) 8014–8021.
[13] W.K. Kim, S.U. Koh, B.Y. Yang, K.Y. Kim, Corros. Sci. 50 (2008) 3336–3342.
[14] S.S. Nayak, R.D.K. Misra, J. Hartmann, F. Siciliano, J.M. Gray, Mater. Sci. Eng. A 494 (2008) 456–463.
[15] G.T. Park, S.U. Koh, H.G. Jung, K.Y. Kim, Corros. Sci. 50 (2008) 1865–1871.
[16] R.A. Carneiro, R.C. Ratnapuli, V. De Freitas Cunha Lins, Mater. Sci. Eng. A 357 (2003) 104–110.
[17] S. Serna, H. Martínez, S.Y. López, J.G. González-Rodríguez, J.L. Albarrán, Int. J. Hydrogen Energy 30 (2005) 1333–1338.
[18] A. Takahashi, M. Iino, ISIJ Int. 36 (1996) 235–240.
[19] B. Beidokhti, A. Dolati, A.H. Koukabi, Mater. Sci. Eng. A 507 (2009) 167–173.
[20] I. Chattora, Sadhana 20 (1995) 199–211.
[21] J.G. Williams, Mater. Forum 31 (2007) 1–10.
[22] J.G. Williams, Thermomechanical Proceeding of Steel, Padua, Italy, 2008.
[23] D.P. Dunne, Mater. Forum 23 (1999) 63–76.
[24] S. Shanmugam, R.D.K. Misra, J. Hartmann, S.G. Jansto, Mater. Sci. Eng. A 441 (2006) 215–229.
[25] S. Shanmugam, N.K. Ramisetti, R.D.K. Misra, J. Hartmann, S.G. Jansto, Mater. Sci. Eng. A 478 (2008) 26–37.

[26] E. Lunarska, Y. Ososkov, Y. Jagodzinsky, Int. J. Hydrogen Energy 22 (1997) 279–284.
[27] Y. Zhong, F. Xiao, J. Zhang, Y. Shan, W. Wang, K. Yang, Acta Mater. 54 (2006) 435–443.
[28] M.-C. Zhao, K. Yang, Scripta Mater. 52 (2005) 881–886.
[29] M.-C. Zhao, K. Yang, Y. Shan, Mater. Sci. Eng. A 335 (2002) 14–20.
[30] K. Junhua, Z. Lin, G. Bin, L. Pinghe, W. Aihua, X. Changsheng, Mater. Des. 25 (2004) 723–728.
[31] A. Contreras, A. Albiter, M. Salazar, R. Pérez, Mater. Sci. Eng. A 407 (2005) 45–52.
[32] L. Reeve, Metal Constr. Br. Weld. J. 6 (1969) 106.
[33] AS 1544.2 Methods for Impact Tests on Metals – Charpy V-notch, 1989.
[34] ASTM E813-89: Standard Method for JIC, A Measure of Fracture Toughness, (1989) pp. 630–634.
[35] ASTM E647-00 Standard Test Method for Measurement of Fatigue Crack Growth Rates, (2000).
[36] http://www.eltragmbh.com/onh2000/information.shtml, 2011.
[37] P. Liang, X. Li, C. Du, X. Chen, Mater. Des. 30 (2009) 1712–1717.
[38] F. Rivalin, A. Pineau, M. Di fant, J. Besson, Eng. Fract. Mech. 68 (2000) 329–345.
[39] A.R. Rosenfield, B.S. Majumdar, Nucl. Eng. Des. 105 (1987) 51–57.
[40] I.M. Bernstein, A.W. Thompson, Int. Met. Rev. 21 (1976) 269–287.
[41] W.M. Cain, A.R. Troiano, Petrol. Eng. 37 (1965) 78.
[42] A.W. Thompson, I.M. Bernstein, Advances in Corrosion Science and Technology, Plenum Press, New York, 1980.
[43] A. Kimura, H.K. Birnbaum, Acta Mater. 36 (1988) 757.
[44] R.D. Calder, T.S. Elleman, K. Verghese, Nucl. Mater. 46 (1973) 46.
[45] T. Tsuru, R.M. Latanision, Scripta Metall. 16 (1982) 575.
[46] M. Ichimura, Y. Sasajima, M. Imabayashi, Mater. Trans. 32 (1991) 1109–1114.
[47] A.J. Haq, K. Muzaka, D.P. Dunne, A. Calka, E.V. Pereloma, Effect of microstructure and composition on hydrogen permeation in X70 pipeline steels, submitted for publication.
[48] L. Tau, S.L.I. Chan, Mater. Lett. 29 (1996) 143–147.
[49] H.-L. Lee, S.L.-I. Chan, Mater. Sci. Eng. A 142 (1991) 193–201.
[50] C.D. Beachem, Metall. Trans. 3 (1972) 451.
[51] W.W. Gerberich, D.D. Stauffer, P. Sofronis, Inter. Hydrogen Conference, 2008, pp. 38–45.
[52] F.B. Pickering, Physical Metallurgy and the Design of Steels, Guildford, Surrey, Great Britain, 1978.
[53] M.A. Arafin, J.A. Szpunar, Corros. Sci. 51 (2009) 119–128.
[54] Y.H. Kim, J.W. Morris, Metall. Trans. A 14 (1983) 1883–1888.
[55] S. Lee, B.C. Kim, D.Y. Lee, Scripta Metall. 23 (1989) 995–1000.
[56] I. Takahashi, Y. Matsumoto, T. Tanada, JIMIS-2, Minakami, Tokyo, Japan, 1979, pp. 285–289.
[57] M.F. Stevens, I.M. Bernstein, Metall. Trans. A 20A (1989) 909–919.
[58] R. Valentini, A. Solina, S. Matera, P.D. Gregorio, Metall. Trans. A 27A (1996) 3773–3779.
[59] F.-G. Wei, K. Tsuzaki, International Hydrogen Conference (ASM International), 2009, pp. 456–463.
[60] M. Garet, A.M. Brass, C. Haut, F. Guttierez-Solana, Corros. Sci. 40 (1998) 1073–1086.
[61] M.-C. Zhao, M. Liu, A. Atrens, Y.-Y. Shan, K. Yang, Mater. Sci. Eng. A 478 (2008) 43–47.
[62] E. Ramírez, J.G. González-Rodriguez, A. Torres-Islas, S. Serna, B. Campillo, G. Dominguez-Patiño, J.A. Juárez-Islas, Corros. Sci. 50 (2008) 3534–3541.
[63] C. Hurtado Noreña, P. Bruzzoni, Mater. Sci. Eng. A 527 (2010) 410–416.